

GT2015-43377

IMPACT OF FLOW NON-AXISYMMETRY ON SWIRLING FLOW DYNAMICS AND RECEPTIVITY TO ACOUSTICS

Samuel Hansford and Jacqueline O'Connor
The Pennsylvania State University
University Park, Pennsylvania

Kiran Manoharan and Santosh Hemchandra
The Indian Institute of Science – Bangalore
Bangalore, India

ABSTRACT

In this study, we experimentally investigate both the intrinsic instability characteristics and forced response to transverse acoustic excitation of a non-reacting, swirling flow for application to combustion instability in annular gas turbine engines. The non-axisymmetry of the velocity field is quantified using an azimuthal mode decomposition of the time-averaged velocity field that shows that (1) the flow field is largely axisymmetric, (2) axisymmetry decreases with downstream distance, and (3) forcing does not significantly alter the time-averaged shape of the flow field. The flow field is analyzed in a companion linear stability analysis that shows that the most unstable modes in the flow field are $m=-1$ and $m=-2$, which agrees with the experimental observations and shows that the intrinsic dynamics of this flow field are non-axisymmetric with respect to the jet axis. The linear stability analysis captures the spatial variation of mode strength for certain modes, particularly mode $m=-1$, but there are some deviations from the experimental results. Most notably, these deviations occur for mode $m=0$ at radii away from the jet axis. Experimental results of the forced response of the flow indicate that the intrinsic instability characteristics of the flow field have an impact on the forced-response dynamics. Response of the flow field to a velocity anti-node in a standing transverse acoustic field shows non-axisymmetric vortex rollup and the dominance of the $m=-1$ and $m=1$ azimuthal modes in the fluctuating flow field. In the presence of a pressure anti-node, the $m=0$ mode of the fluctuating flow field is very strong at the jet exit, indicating an axisymmetric response, and ring vortex shedding is apparent in the flow measurements from high-speed PIV. However, further downstream, the strength of the axisymmetric mode decreases and the $m=-1$ and $m=1$ modes dominate, resulting in a tilting of the vortex ring as it convects downstream. Implications for flame response to transverse acoustic fields are discussed.

NOMENCLATURE

$\bar{B}_{i,m}$	Azimuthal mode shape of the m -th mode
$\hat{B}_{i,m}$	Mode amplitude of Fourier transformed velocity of the m -th mode
D	Outer nozzle diameter
IP	In-phase
OP	Out-of-phase
U_o	Mean/Bulk flow velocity
m	Mode number
r	Radial direction
t	Time
u	Axial velocity component
v	Radial velocity component
x	Downstream distance
\bar{u}_i	Averaged i -direction velocity
\hat{u}'_i	Fourier transform of the fluctuating velocity in i -direction
α	Complex axial wavenumber
θ	Azimuthal direction
ω	Angular frequency
$\omega_{o,i}$	Temporal growth rate at the saddle point

INTRODUCTION

Combustion instabilities in gas turbine engines raise a number of issues for both the development and operation of these machines [1]. Driven by feedback between flame heat release rate oscillations and acoustic fluctuations, combustion instability can result in reduced engine operability, increased emissions, and in extreme circumstances, engine hardware failure [2]. In gas turbines with annular combustion systems, such as those used for aircraft propulsion and some power generation devices, instabilities can arise from coupling

between the flame oscillations and azimuthal, or transverse, modes in the combustion chamber [3].

A number of important issues arise when transverse combustion instabilities are excited. In particular, the coupling pathways between the acoustic oscillations and the flame heat release rate fluctuations may differ from those found during longitudinal instabilities. Work by several authors has outlined the mechanisms by which transverse acoustic fields couple with flame oscillations, and only a brief overview is provided here [4-11].

Flame heat release rate oscillations can arise through a number of pathways, including fluctuations in mixture composition, referred to as “equivalence ratio coupling” [12, 13], and fluctuations in the velocity field, referred to as “velocity coupling” [14-20]. This study focuses on the velocity-coupled pathway of combustion instability, where velocity fluctuations are generated by two sources. First, the acoustic field drives acoustic velocity fluctuations in the region of the flame in both the transverse and longitudinal direction. The transverse oscillations arise from the azimuthal mode, and the longitudinal acoustic fluctuations are generated through an acoustic coupling between the azimuthal mode and the nozzle acoustics [21]. This transverse-to-longitudinal coupling mechanism has been described extensively in the rocket literature, and is referred to there as “injector coupling” [22].

Further, flame heat release rate oscillations can arise from vortical velocity oscillations in the flow field. These oscillations typically stem from the coupling between acoustic oscillations and hydrodynamically unstable portions of the flow field. High swirl-number swirling flows are absolutely unstable, resulting in the breakdown of the jet structure and the formation of a recirculation zone along the centerline of the jet in a process referred to as “vortex breakdown” [23-26]. Studies have shown that high-amplitude acoustic forcing can impact the dynamics of the vortex breakdown bubble, and even lead to flame heat release rate oscillations driven by vortex breakdown motion [20, 27-31].

More typically, though, vortical velocity fluctuations are excited in the shear layers by the presence of acoustic oscillations. Acoustic fluctuations in both the longitudinal and transverse directions can excite vortex rollup at the separation point of the shear layers, and as flames typically stabilize in these shear layers, the vortex rollup and subsequent convection can lead to significant flame disturbance [17-19]. Longitudinal, or axisymmetric, acoustic forcing results in ring vortex rollup at the separation point [18]. However, non-axisymmetric forcing, like that from transverse instabilities, can result in non-axisymmetric response of the shear layers and helical vortex rollup [5, 6, 32]. The dependence of shear layer response on the axisymmetry of the incident acoustic field has been observed in circular jets as well [33, 34].

Even in the absence of acoustic forcing, vortical fluctuations in the shear layers are present in the flow field as a result of naturally occurring hydrodynamic instabilities [35-38]. Swirling flows have multiple shear layers and a vortex

breakdown bubble that are highly susceptible to hydrodynamic instabilities. A swirling flow can have multiple instability mechanisms, which can be broadly classified into (1) shear layer instability, (2) centrifugal instability, and (3) Kelvin instability [38]. The importance of the three instability mechanisms are discussed further in the companion paper by Manoharan *et al.* [39]. Shear layer instability is primarily due to velocity gradients in axial and azimuthal velocity profiles. Unlike in a single, planar shear layer, the shear layer instability in swirling flows is due to the finite shear layer in both the axial and azimuthal velocity profiles. A perturbation can create vortical fluctuations in both the axial and azimuthal vorticity field, which when amplified, results in an unsteady flow. To quantify flow field fluctuations, azimuthal mode decomposition is performed on the velocity field in the r - θ plane. An azimuthal mode decomposition decomposes the flow field into a set of spatially-varying Fourier modes in the azimuthal direction. The mode number quantifies the order of the mode, where $m=0$ is the axisymmetric mode, whereas $m<0$ and $m>0$ are the co-swirling and counter-swirling helical modes, respectively.

The centrifugal and Kelvin instabilities are the result of centrifugal and Coriolis forces in a rotating flows [38]. These forces can have both stabilizing and destabilizing effects depending on the flow field characteristics. Thus the dominant hydrodynamic instability mechanism in a swirling flow is determined by several factors, primarily the shear layer thicknesses in the azimuthal and axial velocity profiles, ratio of the maximum reverse flow velocity magnitude to the maximum axial flow velocity magnitude, and the direction of propagation of unsteady flow perturbations. For example, thinner axial shear layers promote axial shear layer instability. Likewise thinner azimuthal shear layers promote azimuthal shear layer instability. However, the shear layer instability mode dominating the flow dynamics is decided by the orientation of the perturbation wave vector with respect to the axial and azimuthal shear layers. Perturbations along the azimuthal direction promote azimuthal shear layer instability while perturbations along the streamwise direction promote axial shear layer instability. A combination of both these instability mechanisms can result in helical disturbances in the flow field. In general, all these mechanisms, *i.e.*, Kelvin, centrifugal, and shear layer instability mechanisms, interact, potentially resulting in an unsteady, non-axisymmetric flow.

Instability characteristics of spatially developing flows can be classified on the basis of their response to an impulsive forcing at a point in the flow field at large times [40]. If the impulsive forcing results in disturbances being convected away from the point of forcing and growing spatially, then the flow is said to be a convectively unstable flow. This kind of flow requires continuous forcing to sustain flow unsteadiness. In absolutely unstable flows, impulsive forcing results in both temporal and spatial disturbance growth. This kind of flow continues to sustain flow unsteadiness without external forcing, hence these flows acts like self-excited oscillators. Absolute/convective instability characteristics are a strong

function of the time-averaged traits of the flow field. In particular, for a swirling flow, shear layer thickness, backflow ratio, and swirl number all impact the stability boundary. Several prior studies have reported the influence of swirl on the absolute/convective nature of the flow field [36, 37, 41-43].

In this work, we systematically quantify the time-averaged characteristics, the natural instability modes, and the forced response of a swirling flow subjected to transverse acoustic forcing, like would be seen during an azimuthal instability. Experimental results measured with high-speed particle image velocimetry (PIV) are compared with linear stability calculations to better understand the natural hydrodynamic instabilities of the flow field and how these natural modes impact the response of the flow to both axisymmetric and non-axisymmetric acoustic forcing.

The remainder of the paper is organized as follows. First, we provide an overview of the experimental and analytical techniques used. Next, the time-averaged characteristics of the flow field are discussed to provide a baseline for the dynamical results, and to quantify how closely the experimental data matches the input velocity field assumptions required for the linear stability predictions. Both experimental results and linear stability prediction of the natural dynamics of the flow field are presented, and the paper concludes with a discussion of the forced response dynamics.

EXPERIMENTAL OVERVIEW AND ANALYSIS

These experiments were performed in a transverse forcing facility capable of creating standing-wave transverse acoustic excitation. This experimental setup has been described in previous works [4, 29]. The experiment was designed for excitation frequencies between 400 Hz and 2000 Hz, a typical frequency range for combustion instabilities in annular gas turbines. Acoustic modeling indicates that the transverse wave in this facility is one-dimensional up to a frequency of approximately 1200 Hz, after which the longitudinal mode of the combustor is also excited, resulting in a mixed-mode. The combustor is shown in Figure 1.



Figure 1. Transverse forcing experiment.

Before entering the combustor, the flow passes through a large settling chamber with perforated plates. The chamber acts to both break up large coherent structures upstream of the combustor and acoustically decouple the combustor acoustics and the air and fuel supply. The flow enters the combustion chamber through a 12-bladed swirler with a blade angle of 45

degrees, resulting in a geometric swirl number of 0.85 [44]. The nozzle has a diameter of 3.175 cm and contains a cylindrical centerbody with diameter of 1.09 cm that is flush with the dump plane.

The high aspect ratio combustor is 114.3 cm in the transverse direction, 35.56 cm in the longitudinal direction, and 7.62 cm wide. The design mimics an unwrapped annular combustor, retaining the boundary conditions of the flame with strong confinement on two sides and open conditions on either side. The current experiment only considers one swirling flow, so that the boundary condition on either side of the flame in the transverse direction is quiescent air, unlike a real combustor where there would be adjacent flames on either side. Recent studies have shown that single flame dynamics in a transverse forcing facility can reasonably mimic those of a flame in a multi-flame [8] or annular combustor [45]. The necessary conditions to make this comparison are explained in Ref. [45].

The bulk velocity, U_o , through the combustor is 10 m/s. The bulk velocity was determined by taking the mass flow rate and dividing it by the area of the nozzle times the reactant density. Transverse acoustic forcing was supplied by six drivers, three on each side of the combustor at the end of 1-meter long adjustable tubes. Two standing-wave modes were investigated in this study, the axisymmetric and non-axisymmetric conditions. At the axisymmetric condition, the speakers are forced “in-phase” and an approximate pressure anti-node is created at the centerline of the combustor. Forcing the speakers 180 degrees “out-of-phase” results in a non-axisymmetric forcing condition with an approximate velocity anti-node along the centerline. The out-of-phase forcing frequencies have velocity fluctuations near 40% of the mean flow velocity and the in-phase forcing has velocity fluctuations that are close to 5% the mean flow [29]. Wavelengths for the 400 and 800 Hz frequencies are 0.86 meters and 0.43 meters, respectively, while the nozzle is only 0.0318 meters; the nozzle is acoustically compact. More details of these forcing conditions can be found in O’Connor and Lieuwen [32].

Diagnostics

The flow field was measured using high-speed particle image velocimetry (PIV). The high-speed PIV was taken at 10 kHz with a Litron LDY303He Nd:YLF laser and an SA1.1 Photron camera at a resolution of 0.14 mm/pixel. One to two micron seeding particles of alumina were used for flow tracking. The data were taken in two planes. One we term the r - x plane, where the two-dimensional PIV measures the axial and radial components of velocity, and the other we term the r - θ plane where the radial and azimuthal velocity components are measured.

The PIV calculations were performed with LaVision’s DaVis 7 with a final interrogation window size of 16x16. The calculation was made with a three-point Gaussian fit and a three-pass calculation; the first pass at an interrogation window size of 32x32 and the second two passes with a size of 16x16. During post-processing, vectors were rejected based on three

criteria. First, velocity vectors with magnitudes greater than 25 m/s were deemed unphysical for this flow. Second, median filtering was used to filter points where surrounding velocity vectors had an RMS value greater than three times the local point. This filter is used to rid the field of spurious vectors that occur due to issues with imaging. A third outlier detection scheme was also used that removed groups of outlier vectors; this operation removes errors caused by local issues with the original image, including window spotting, and are aggravated by using overlapping interrogation windows. The rejected vectors were replaced with interpolated values; on average, 8% of the vectors were removed and replaced.

Data Analysis

The flow dynamics quantified in this work can best be described in cylindrical coordinates, where radial and azimuthal velocity fluctuations are significant metrics for jet instability. However, PIV inherently uses a Cartesian coordinate system, so a transformation to cylindrical coordinates is required in the r - θ plane. To transform the velocity field from Cartesian to cylindrical coordinates, each component of velocity is interpolated using a spline scheme onto a cylindrical coordinate system with 21 radial increments and 180 azimuthal increments. Similar spatial resolution between the Cartesian and cylindrical coordinates is maintained as much as possible. The resultant interpolation points are shown in Figure 2. This figure shows the velocity magnitude normalized by the bulk velocity with the interpolation points. The velocity magnitude is given by:

$$U_{Mag} = \sqrt{u_r^2 + u_z^2} \quad (1)$$

The flow field center (and interpolation origin) was found manually at $x/D=0$, and was maintained at each downstream position. Numerous comparisons were made between the original Cartesian and interpolated data to ensure that important characteristics of the velocity field were not distorted by the interpolation. These comparisons are not shown.

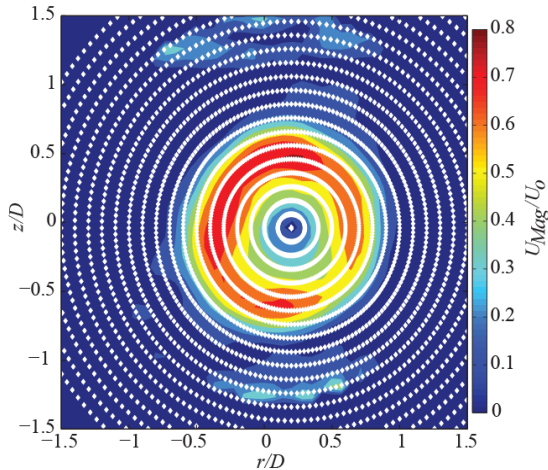


Figure 2. Interpolation points (white diamonds) shown with the velocity magnitude in the r - θ plane at $x/D=0$.

Recent work has shown that axisymmetry of the time-averaged velocity field plays an important role on the response of flames to acoustic forcing [9]. In this work, we use a harmonic azimuthal decomposition to quantify the level of axisymmetry of the time-averaged flow field, as shown in Eq. 2.

$$\bar{B}_{i,m}(r, x) = \frac{1}{2\pi} \int_0^{2\pi} \bar{u}_i(r, x, \theta) e^{-im\theta} d\theta \quad (2)$$

Here, $\bar{B}_{i,m}$ is the strength of mode m of the time-averaged velocity component i . Mode $m=0$ has an axisymmetric shape, while modes $m \neq 0$ are non-axisymmetric shapes; these shapes follow those from acoustic theory [46]. For example, if the magnitude of $\bar{B}_{i,m=0}$ is much larger than any other $\bar{B}_{i,m \neq 0}$, then the flow field is highly axisymmetric in a time-averaged sense. However, if any $\bar{B}_{i,m \neq 0}$ has a significant amplitude, then the time-averaged velocity component, \bar{u}_i , is non-axisymmetric with a shape given by m .

The dynamic behavior of the velocity field is quantified in both the frequency and azimuthal mode domains. A Fourier transform is applied to each component of the velocity field, resulting in a 20 Hz spectral resolution and a maximum resolvable frequency of 5000 Hz. Additionally, an azimuthal mode decomposition is used to quantify fluctuations in the r - θ plane, as shown in Eq. 3. This decomposition is similar in form to the decomposition in Eq. 2, but here the Fourier transformed fluctuating velocity is transformed, resulting in azimuthal mode strengths, $\hat{B}_{i,m}$, that quantify the modal dynamics of fluctuating velocity components, not the shape of the flow field. These mode strengths can be calculated for different velocity components, i , and at different frequencies, ω , to understand both the spatial and temporal dynamics of the flow field.

$$\hat{B}_{i,m}(r, x, \omega) = \frac{1}{2\pi} \int_0^{2\pi} \hat{u}'_i(r, x, \theta, \omega) e^{-im\theta} d\theta \quad (3)$$

In Eq. 3, \hat{u}'_i is the Fourier-transformed fluctuating velocity component in direction i . This decomposition will allow the measurements of instability modes in the flow to be compared to the predictions from linear stability analysis.

It is important to note the differences in the physical interpretations of the azimuthal decompositions in Eq. 2 and Eq. 3, despite the similarities in mathematical formulation. The set of $\bar{B}_{i,m}$ from Eq. 2 describes a time-averaged shape and should not be thought of as “modes” in the oscillating sense. It is natural to decompose a swirling flow field into azimuthal components, and the time-averaged shape strengths, $\bar{B}_{i,m}$, provide quantitative information about the level of axisymmetry in the time-averaged flow field. This method is also consistent with recent work on the dynamics of non-axisymmetric flames by Acharya and Lieuwen [9, 47], where the time-averaged flame

shape is quantified in this same manner. On the other hand, the fluctuating mode strengths, $\hat{B}_{i,m}$, describe the amplitude and phase of spatial modes of fluctuating velocities.

Linear Stability Analysis

In the present study, an inviscid, low Mach number, local hydrodynamic stability analysis is performed using the experimentally measured, time-averaged velocity fields as the base flow. The well-posedness of stability analysis on a time-averaged velocity field is a topic of current research, but prior studies using the same approach have shown qualitatively and quantitatively accurate predictions [43]. We provide an overview of the formulation of this analysis in this section. The reader is referred to a companion paper [39] for a more detailed description.

The base flow is assumed to be axisymmetric. Also, the radial component of base flow velocity is neglected because the maximum magnitude of the radial component of the base flow velocity was found to be negligible when compared with other base flow velocity components in the present study. The base flow is assumed to be locally parallel (*i.e.*, does not vary in the axial direction). The Navier-Stokes equations in cylindrical coordinates are linearized about the time-averaged axisymmetric base state to obtain the linearized Navier-Stokes (LNS) equations [39]. The perturbation quantities in the LNS equations at the $r \rightarrow \infty$ limit are assumed to be zero. An auxiliary kinematic boundary condition is also imposed at the centerline as derived by Batchelor *et al.* [48]. All perturbation quantities are written in the normal mode form, $q'(r, \theta, x, t) = \hat{q}(r) e^{i(\alpha x + m\theta - \omega t)}$, where, q' is a vector of perturbation quantities and $\hat{q} = \{\hat{\rho}, \hat{u}_r, \hat{u}_\theta, \hat{u}_x, \hat{p}\}$. The quantities α and m corresponds to the axial wavenumber and azimuthal wavenumber respectively. Thus, the LNS equations, along with the boundary conditions, yield an eigenvalue problem in terms of α , m and ω . This essentially amounts to solving a dispersion relation between these quantities. The real part (α_r) is the axial wavenumber and the imaginary part (α_i) is the spatial growth rate. Likewise, ω is the temporal eigenvalue, where the real (ω_r) and imaginary (ω_i) parts corresponds to the real frequency and temporal growth rate, respectively. In general, the dispersion relation relates the spatial and temporal eigenvalues for a given azimuthal wavenumber (m).

This eigenvalue problem cannot be solved in closed form for a general base-flow. Therefore, we use the Chebyshev pseudospectral collocation method to solve this problem numerically. The physical space, $r \in [0, 2]$ is mapped onto the computational space $[-1, 1]$ using a transformation function suggested by Malik *et al.* [51]. Next, the LNS are discretized on the computational space at Chebyshev collocation points using cardinal functions [52], yielding a discrete equivalent of the exact eigenvalue problem. The base flow velocity profile in the present study is obtained by fitting to the time-averaged velocity in the $r-\theta$ plane to the velocity model suggested by from

Oberleithner *et al.* [43] using least-squares curve fitting. The curve fit allows for smoothing of the experimental noise as well as interpolation of the data on to the Chebyshev collocation points. The number of collocation points as well as the parameters in the mapping function are adjusted so that the change in the real and imaginary part of the computed eigenvalues is less than 0.01%. As such, 100-150 collocation points were found to be necessary to achieve this level of convergence. We perform temporal and spatio-temporal analyses in this paper in order to identify unstable modes as well as their absolute/convective nature at three axial locations in the experimental dataset. We use the algorithm suggested by Deissler [49] to identify the saddle points in the complex α -plane as needed by the spatio-temporal analysis in order to determine the nature of the flow instability.

RESULTS

Time-Averaged Flow Field

The flow field in this study has been discussed in earlier work [29]. Figure 3 shows the time-averaged velocity field on the left, and out-of-plane vorticity on the right in the $r-x$ plane. The velocity is normalized by the bulk velocity, U_o , and the vorticity is normalized by the bulk velocity divided by the nozzle diameter, D . The streamlines show a noticeable difference between the left and right half of the flow field as a result of the non-axisymmetry of the flow field, which is quantified in this section. Here, an annular jet flows around a recirculation zone and forms two shear layers. The outer shear layer results from mixing of the jet with the ambient quiescent fluid, and the inner shear layer results from mixing of the jet with the reverse flow in the vortex breakdown region.

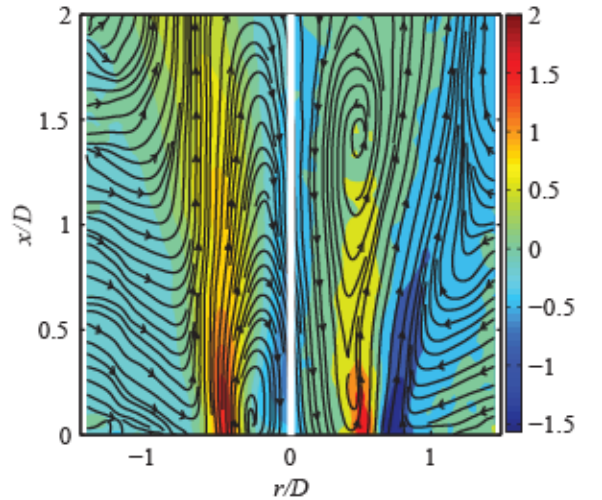


Figure 3. Non-dimensionalized time-averaged velocity (left) and vorticity (right) in the $r-x$ plane with mean flow velocity of $U_o=10$ m/s, swirl number of 0.85. Colorbar applies to both normalized velocity and vorticity.

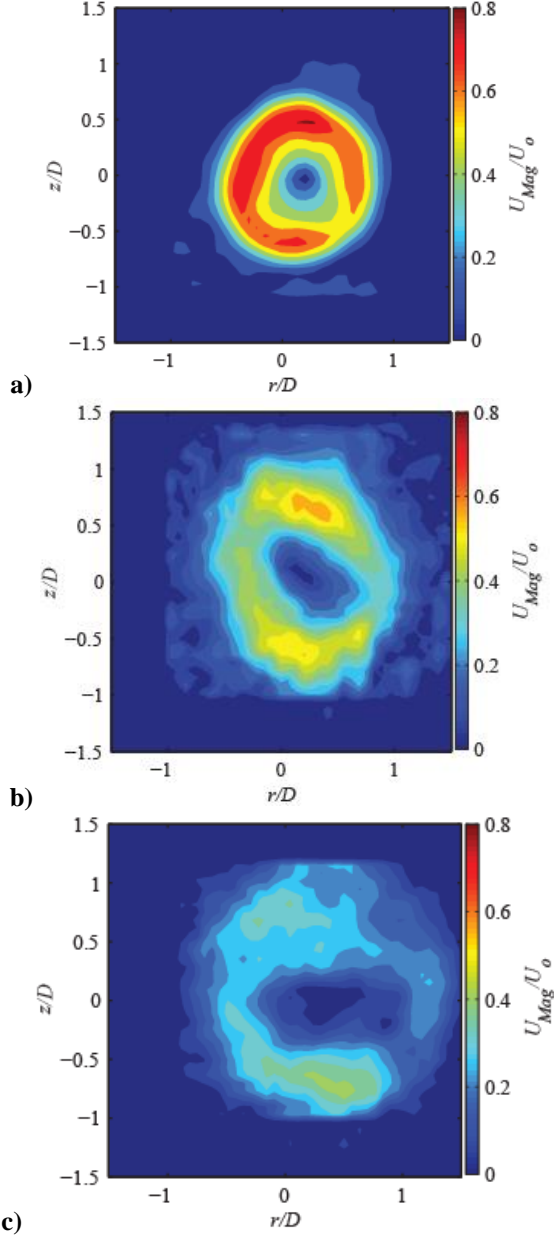


Figure 4. Time-averaged velocity magnitude in the r - θ planes at three downstream locations: a) $x/D=0$, b) $x/D=1$, and c) $x/D=2$, with mean flow velocity of $U_o=10$ m/s, swirl number of 0.85

Figure 4 shows the magnitude of the velocity in the r - θ plane at three downstream distances. The high velocity of the swirling jet core is evident at each downstream location, as is the low-velocity center of the jet. It is evident from the velocity magnitude plots in the r - θ plane that the axisymmetry of the time-averaged flow field varies as a function of downstream distance. At $x/D=0$, the flow field is relatively axisymmetric as the jet first exits from the axisymmetric nozzle. As the flow progresses downstream, however, the influence of the high aspect ratio combustor shapes the flow so that the jet is

somewhat elliptical by $x/D=2$. We quantify the non-axisymmetry using the azimuthal decomposition described in Eq. 2. Figure 5 shows the results of the azimuthal shape decomposition on the time-averaged azimuthal and radial velocity components.

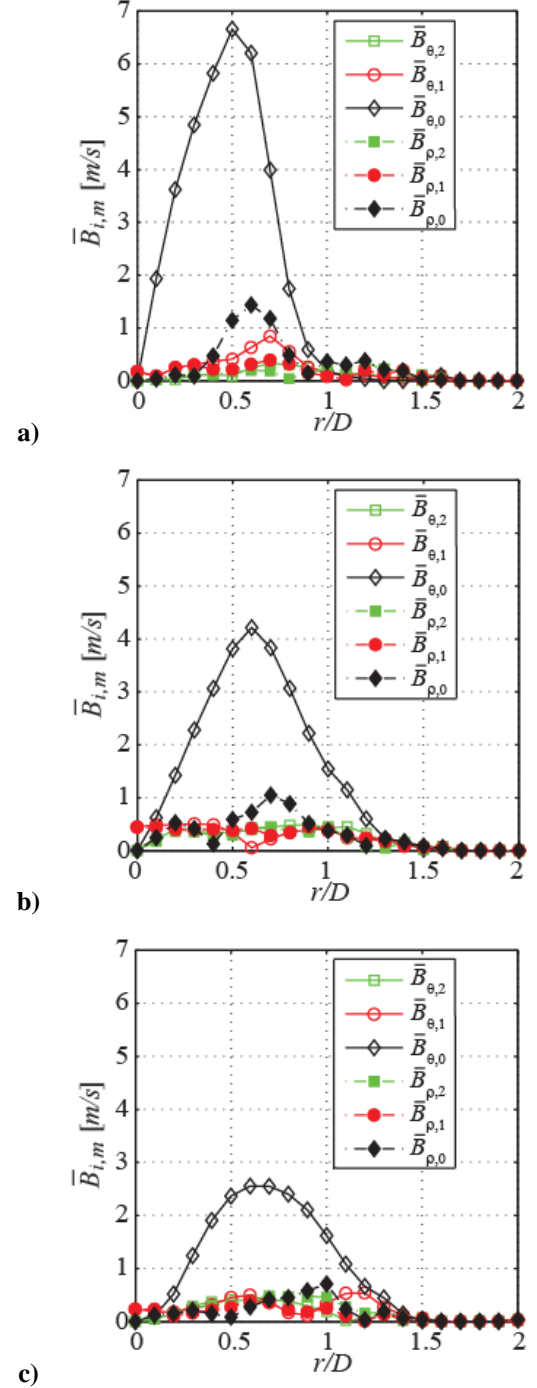


Figure 5. Time-averaged shape quantified with the azimuthal mode decomposition at a) $x/D=0$, b) $x/D=1$, and c) $x/D=2$ for azimuthal velocity (open symbols) and radial velocity (filled symbols).

The azimuthal shape modes in Figure 5 quantify the time-averaged axisymmetry of the jet. At all three downstream locations, the $m=0$ shape mode is significantly larger than the other modes, indicating the jet is largely axisymmetric on average. The results show that the annular jet core is located near $r/D=0.5$, as can be seen by the high velocities in that region. As the flow progresses downstream, the jet spreads radially outwards and the velocity decays, decreasing the strength the $m=0$ mode in particular. The strengths of the non-axisymmetric shape modes decrease less dramatically with downstream distance than the axisymmetric shape modes, indicating that the non-axisymmetric contributions have a greater relative importance away from the dump plane. This is likely the result of the non-axisymmetric wall boundary conditions that confine the jet in the high aspect ratio combustor. The radial velocity displays similar behavior to the azimuthal velocity except at a much lower magnitude; this indicates that the swirling velocity component is much stronger than the radial velocity component.

There are two key assumptions in the accompanying linear stability analysis that relate to the time-averaged shape of the flow field. The first is that the time-averaged flow field is axisymmetric, and the second is that the radial velocity is zero. The results of this azimuthal shape decomposition show that these assumptions are generally applicable to this flow field.

In this section we further discuss shape modes between $m=-2$ and $m=2$ because they contain most of the energy. In the azimuthal mode decomposition, modes $m=-10$ to $m=10$ are calculated, but the amplitude of the modes outside the $m=-2$ to $m=2$ range are very low. To show this, the sum of modes $m=-2$ to $m=2$ and the sum of modes $m=-10$ to $m=10$ are presented in Figure 6 for 400 Hz IP forcing, 400 Hz OP forcing, and no forcing. These three cases are the main focus of this study. Here, the sum of mode strengths for $m=-2$ to $m=2$ are shown as symbols, and the sum of mode strengths for $m=-10$ to $m=10$ are shown in dotted lines. Both mode ranges are plotted from $r/D=0.1$ to $r/D=1.5$. These limits are chosen because $r/D=0$ is a singularity and the modal decomposition does not work at this point; therefore, $r/D=0.1$ is the lower limit. The upper limit, $r/D=1.5$, is the outer edge of the jet at both $x/D=1$ and $x/D=2$. The edge of the jet at $x/D=0$ is $r/D=0.9$ (see Figure 2). For all radii, modes $m=-2$ to $m=2$ contain the majority of the total modal strength; therefore, using modes $m=-2$ to $m=2$ captures most of the time-averaged mode energy.

Figure 7 distills some of the important results from Figure 5, and shows the amplitude of azimuthal shape modes, from $m=-2$ to $m=2$, at three key radial positions as a function of downstream distance. The position $r/D=0.2$ is located inside the vortex breakdown bubble, $r/D=0.4$ is located at the inner shear layer, and $r/D=0.6$ is located at the outer shear layer. These locations were determined by inspecting the r - x plane as in Figure 3. Please note that to make the mode strengths clearer, the radial velocity the ordinate upper limit is 1.5 m/s, while for the azimuthal velocity the upper limit is 8 m/s.

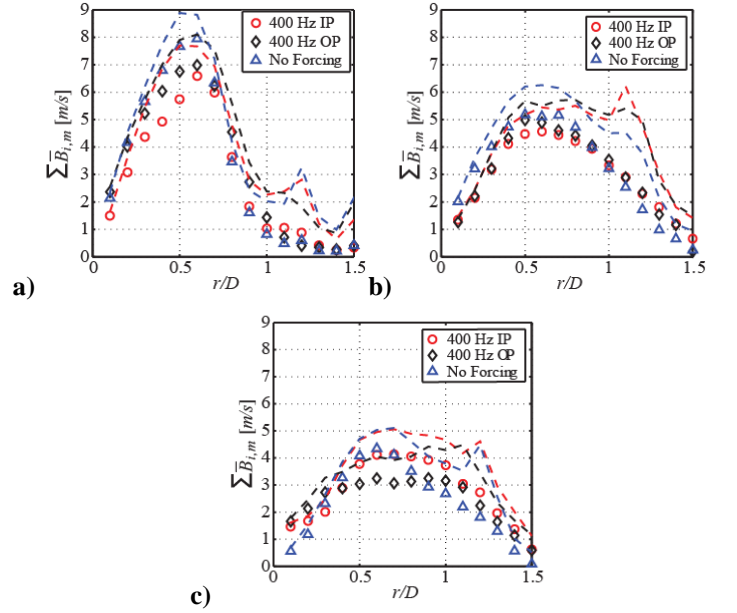


Figure 6: Sum of time-averaged mode strengths from modes $m=-10$ to $m=10$ (dashed line) and modes $m=-2$ to $m=2$ (symbols) for 400 Hz IP forcing, 400 Hz OP forcing, and no forcing at a) $x/D=0$, b) $x/D=1$, and c) $x/D=2$.

A number of features are evident from these plots. First, the strength of the axisymmetric azimuthal shape mode, $m=0$, is greater than all other modes, indicating that the axisymmetric assumption in the linear stability analysis applies relatively well to this flow field. This decomposition gives us a quantitative way to assess this assumption, showing the relative strengths of the modes as a function of downstream distance. From these relative strengths, it is evident that the assumption breaks down further downstream, where the strength of the axisymmetric shape mode is only 2.5 times that of modes $m=1$ and $m=-1$ at $x/D=1$ in the vortex breakdown bubble.

Further, the time-averaged radial velocities in all shape modes are much less than the azimuthal velocities. In this combustor the bulk motion of the swirl is much larger than the jet spread; therefore, the time-averaged strength of the azimuthal velocity is much stronger than the radial velocity. However, the time-averaged radial velocity profiles are much less axisymmetric than the azimuthal velocity profiles.

The application of acoustic forcing does not appreciably change the time-averaged azimuthal shape modes. Figure 8 shows an example of the azimuthal shape modes for a number of acoustic forcing conditions, including two forcing frequencies, 400 Hz and 800 Hz, and both in-phase and out-of-phase acoustic forcing. In the out-of-phase forcing cases, the transverse acoustic velocity fluctuation amplitude was approximately 4 m/s, $v'/U_o=0.4$, and the acoustic drivers were run at the same amplitude for the in-phase forcing cases, although the centerline acoustic velocity fluctuation is negligible in this case as a velocity node is present. Numerous

studies have shown that these forcing conditions can impact the dynamic behavior of the flow field [4, 6], but the time-averaged flow behavior between the no forcing and forcing cases is similar. These cases stay away from a flow-field bifurcation behavior that was observed by O'Connor and Lieuwen [29] at 800 Hz out-of-phase forcing at very high forcing amplitudes.

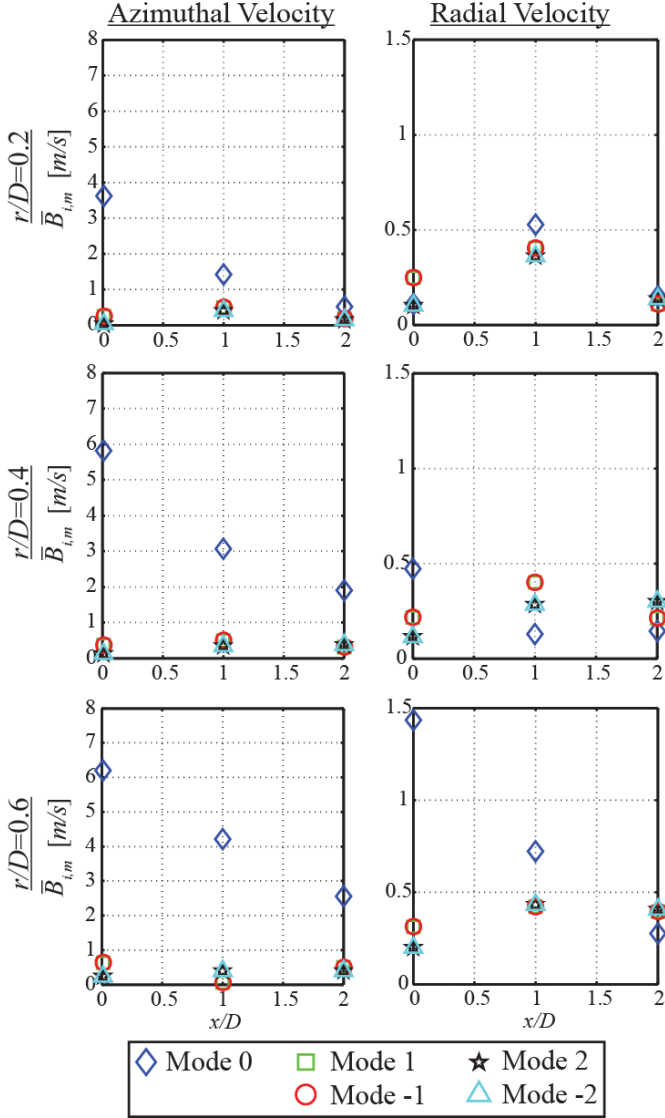


Figure 7. Azimuthal shape modes of the time-averaged azimuthal and radial velocities for $m=-2$ to $m=2$. The first row is $r/D=0.2$, second row is $r/D=0.4$, and third row is $r/D=0.6$.

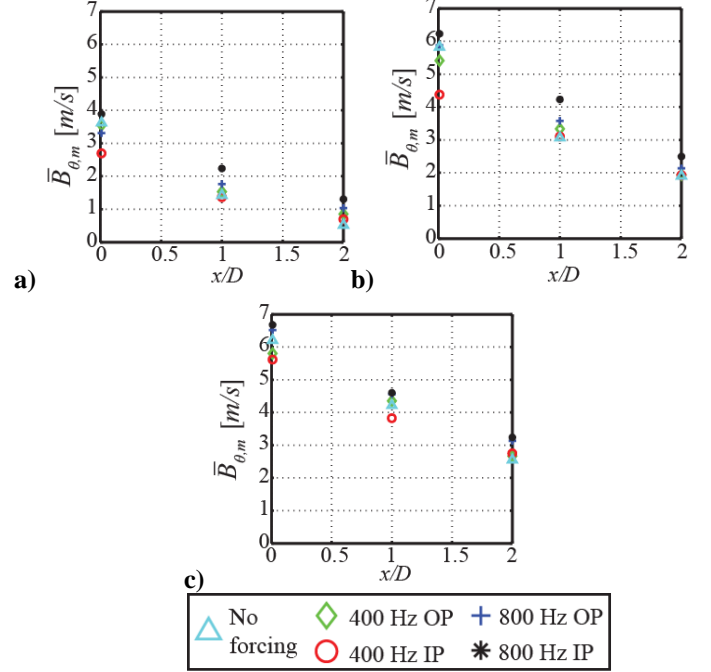


Figure 8. Azimuthal shape modes for mode $m=0$ for all time-averaged flows in this study at a) breakdown bubble ($r/D=0.2$), b) inner shear layer ($r/D=0.4$), and c) outer shear layer ($r/D=0.6$).

Self-Excited Dynamics

Several researchers have reported on various aspects of the natural dynamics of swirling flows [29, 35, 50]. The self-excited dynamics of this particular flow field were analyzed extensively in O'Connor and Lieuwen [29], and only pertinent results are presented here as a baseline of comparison to the forced response results below. Low frequency content, less than 200 Hz, dominates the natural swirling dynamics for this flow field. The dynamics are quantified here using the azimuthal mode decomposition described in Eq. 3, where the velocity fluctuations have been integrated over frequency space before being transformed into azimuthal modes.

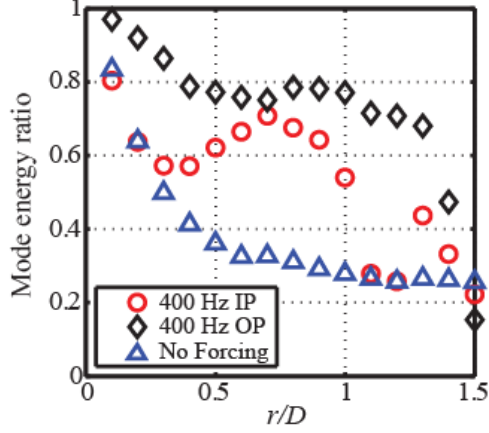


Figure 9. Ratio of mode energy in modes $m=-2$ to $m=2$ to mode energy in modes $m=-10$ to $m=10$ for $x/D=0$ at a range of radial positions and forcing conditions.

Modes $m=-2$ to $m=2$ are studied in the dynamics portion of this paper because of the important dynamical features that contain these modes, as will be explained in this section. Figure 9 shows the ratio of the mode energy from $m=-2$ and $m=2$ divided by the total mode energy at $x/D=0$. At $x/D=0$, much of the energy is concentrated between modes $m=-2$ and $m=2$ in the inner region of the flow field, although this ratio decreases significantly at the edge of the jet, particularly for the no-forcing case. Similar trends are seen at $x/D=1$ and $x/D=2$.

The modal decomposition of the fluctuating flow field is shown in Figure 10. The mode strengths are shown at three radial locations and for three downstream stations. The mode strength of the fluctuating velocity is an order of magnitude smaller than the time-averaged mode strengths, indicating that the velocity fluctuations are on the order of 10% of the mean flow velocity. In the vortex breakdown bubble, at $r/D=0.2$, the magnitudes of the velocity fluctuations at all mode numbers increase from $x/D=0$ to $x/D=1$ but either decrease or stagnate from $x/D=1$ to $x/D=2$. The fluctuating radial and azimuthal velocities both exhibit this nonmonotonic behavior. At all three radial locations, modes $m=-2$ and $m=-1$ are dominant. This behavior was seen in O'Connor and Lieuwen and was attributed to a precessing vortex core motion [29]. Mode $m=-1$ is related to helical motion inside the bubble, while mode $m=-2$ is related to jet deformation.

The stability of modes $m=-2$ through $m=2$ from the spatio-temporal stability analysis is shown in Figure 11. Modes $m=-1$ and $m=-2$, non-axisymmetric modes, are both absolutely unstable, and the amplitude of the growth rate shows a non-monotonic behavior with downstream distance. Modes $m=0$, $m=1$, and $m=2$ are convectively unstable, but not absolutely unstable.

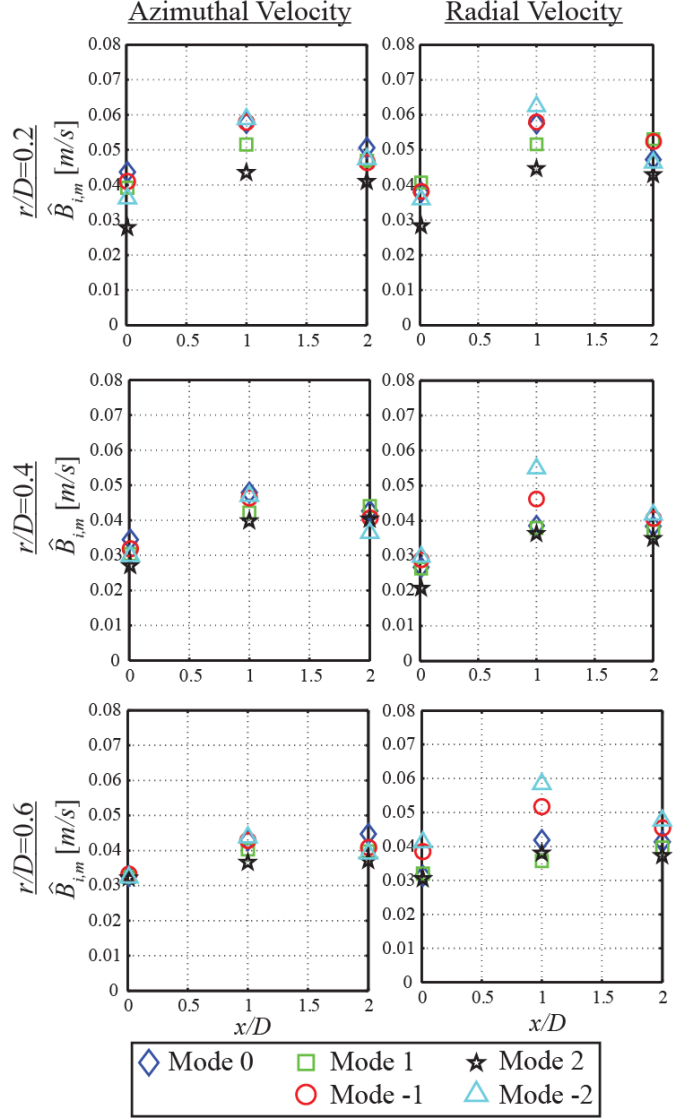


Figure 10: Azimuthal modes, $m=-2$ to $m=2$, at three radial positions for unforced swirling flow with mean flow velocity of $U_o=10$ m/s, swirl number of 0.85

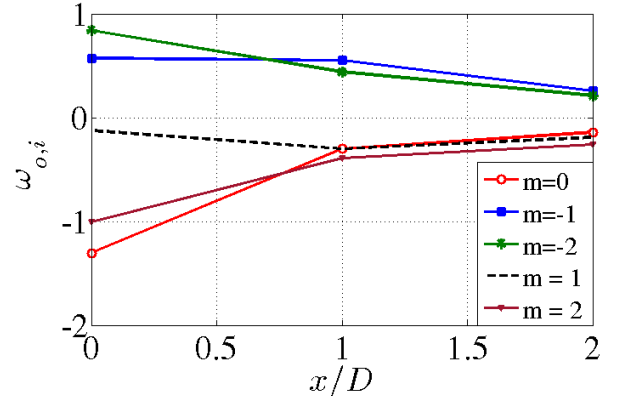


Figure 11. Linear stability analysis prediction of the growth rate of modes $m=-2$ to $m=2$ at three downstream distances.

The stability analysis also provides the strength of modes $m=-2$ to $m=2$ as a function of radius at the three downstream positions. Mode $m=-1$ predictions are compared to the experimental data in Figure 12, while modes $m=0$ and $m=-2$ predictions are displayed in Figure 13. The stability analysis predicts the modal strength for all three velocity components, while the experimental data only has the azimuthal and radial velocities. Therefore, the modal strength of the predicted axial velocity fluctuations is removed. As a result, only the shapes of the modes should be compared between the prediction and the experimental results, instead of quantitative mode strengths.

In Figure 12, the comparison between the experimental results and stability predictions is presented for mode $m=-1$. The solid lines are the stability calculations and the dashed lines with symbols are the experimental data. The azimuthal mode decompositions of the azimuthal velocity are in red and the radial velocity are in blue. The stability calculations agree well with the experimental results inside the breakdown bubble, $r/D \leq 0.3$. Outside the breakdown bubble, mode $m=-1$ decreases in both the stability predictions and the experimental results.

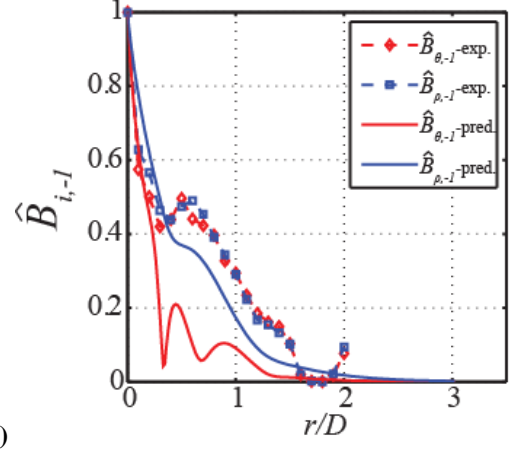
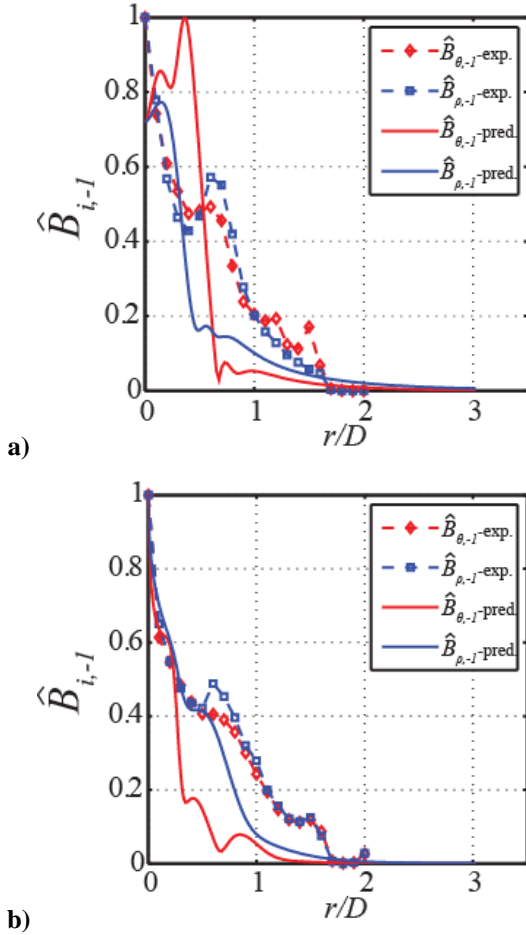


Figure 12: Comparisons between linear stability analysis (solid line) and experimental data for mode $m=-1$ at a) $x/D=0$ b) $x/D=1$ c) $x/D=2$ at all radii.

Stability calculations under-predict the strength of the mode $m=-1$ in the shear layers at $r/D > 0.3$. The local peak in the experimental data around the outer shear layer, near $r/D=0.6$, indicates that the shear layers contain helical modes but the stability predictions do not capture this quantitatively, but do so qualitatively. Both the experimental data and stability calculations indicate that the edge of the jet is located near $r/D=2$ because velocity fluctuation levels go to zero.

Figure 13 shows the comparisons between the experimental data and the stability analysis for modes $m=0$ and $m=-2$, using the same formatting as Figure 12. The same three downstream distances are plotted, $x/D=0, 1$, and 2 , and modal strengths are plotted out to $r/D=3$. Here, the stability predictions identify several important features but there is more deviation from the experimental results than the calculations for mode $m=-1$. For mode $m=0$, there are local peaks in the shear layers for both experimental and stability predictions. The outer shear layer, at $0.6 < r/D < 1$, is stronger than the inner shear layer, at $0.3 < r/D < 0.5$, at $x/D=0$. Stability calculations show that the inner shear layer fluctuations become stronger than the outer shear layer fluctuations between $x/D=1$ and $x/D=2$, whereas in the experimental data, the inner shear layer fluctuations begin to dominate at $x/D=1$. In the jet core, near $r/D=0.5$, the stability analysis predicts a sharp decrease in the strength of mode $m=0$, whereas in the experimental results the local minima is not as severe. These minima indicate that velocity fluctuations in the jet core are relatively smaller than those in the shear layers, which is consistent with physical mechanism driving the instability, which is fluid shear.

For mode $m=-2$, the maximum mode strength occurs inside the breakdown bubble for both the predicted and experimental results, and the predicted shape of the mode in this region is quite accurate. The stability calculation deviates from the experimental data outside the vortex breakdown region, $r/D \leq 0.3$, as the predicted mode strength decays more strongly than the measured mode strength with radial distance. The peak

in the $m=-2$ mode in the outer shear layer, near $r/D=0.6$, is not predicted in the stability analysis.

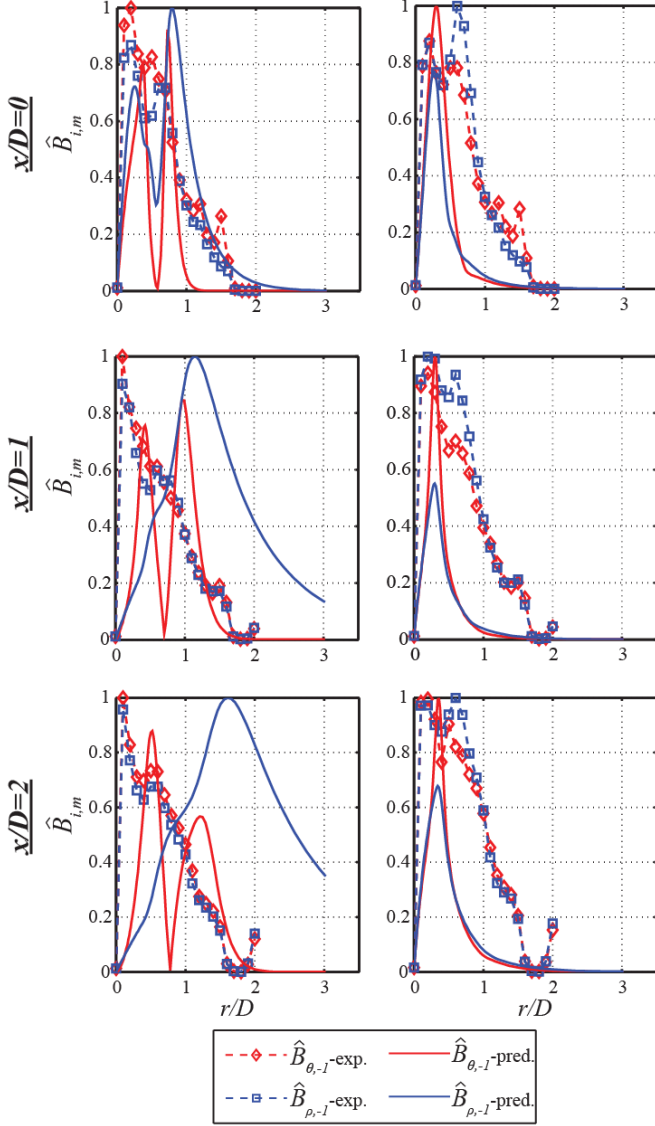


Figure 13: Comparisons between linear stability analysis (solid line) and experimental data for modes $m=0$ (left) and $m=-2$ (right) at a) $x/D=0$, b) $x/D=1$, and c) $x/D=2$.

Overall, the stability predictions are able to capture the trends of the experimental data. The predictions correctly capture the mode numbers of the absolutely unstable modes, $m=-1$ and $m=-2$. The experimental results show that these absolutely unstable modes have local peaks in the shear layers but the stability prediction does not always capture this. There are some deviations from the experimental data, most notably that the stability analysis predicts narrow peaks in mode strengths inside the shear layers whereas the data varies much less dramatically. Also, the prediction of the radial velocity fluctuations are poor relative to the azimuthal velocity fluctuation. To increase the accuracy of the linear stability

analysis, the axisymmetric assumption will be relaxed in future work.

Forced Response

The forced response of the flow field is highly dependent on the forcing conditions. The response of the flow field to acoustic forcing is quantified using the azimuthal mode decomposition on the Fourier-transformed velocity field at the forcing frequency and visualized by comparing the instantaneous and phase-averaged vortex roll-up in the velocity data. The flow response to non-axisymmetric, out-of-phase, forcing has strong non-axisymmetry with respect to the jet axis. Different mode strengths for the vortex breakdown region, inner shear layer, and outer shear layer are presented in Figure 14, and the visualization of the velocity field is shown in Figure 15.

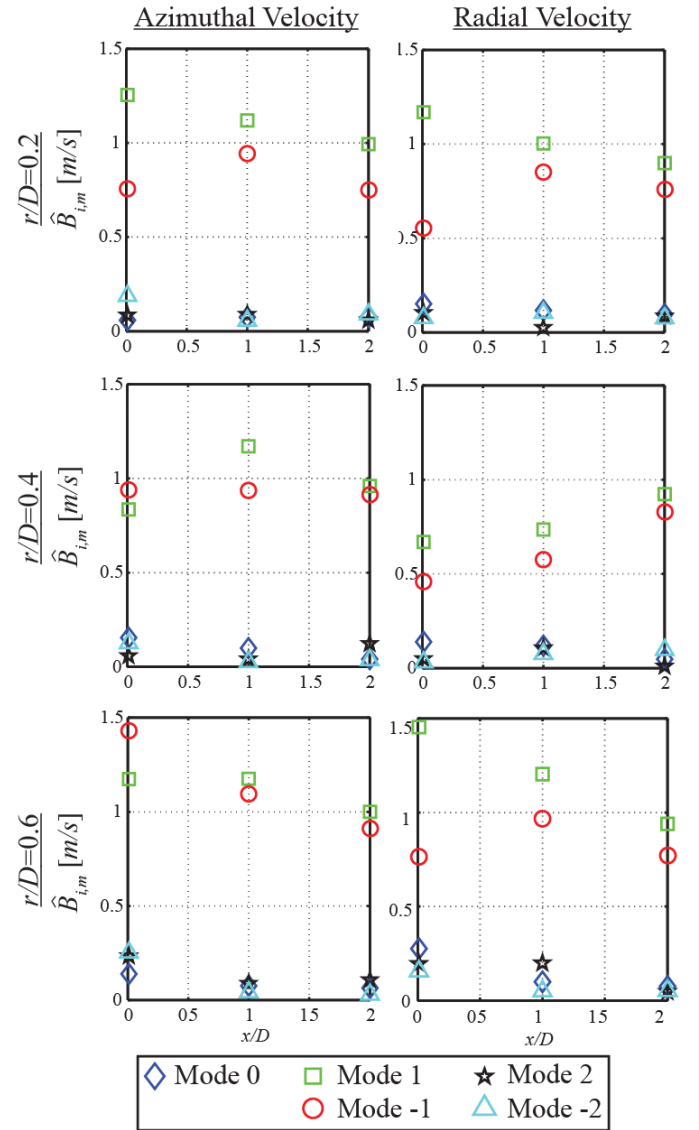


Figure 14: Azimuthal modes, $m=-2$ to $m=2$, at three radial positions for 400 Hz out-of-phase forcing with mean flow velocity of $U_o=10$ m/s, swirl number of 0.85.

The response does not vary greatly between different radii. Modes $m=-1$ and $m=1$ are dominant across the flow field at a range of radial and downstream positions. This non-axisymmetric fluctuating energy is a result of both the non-axisymmetric acoustic velocity fluctuations as well as the non-axisymmetric shear layer oscillations. The physical manifestation of the shear layer oscillation is helical vortex roll-up, which is evident in both the instantaneous and phase-average velocity fields in Figure 15. Notional representations of the helical shape of the vortex roll-up are shown as well.

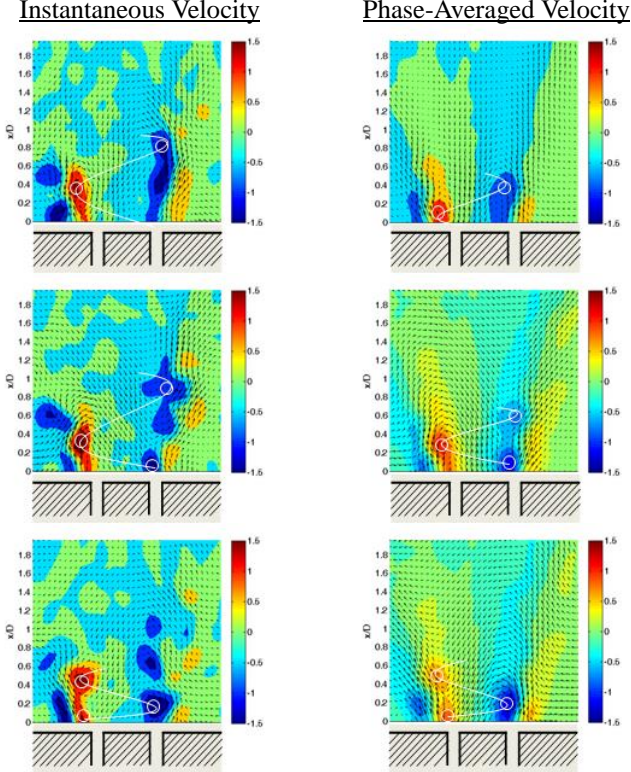


Figure 15. Normalized velocity (vectors) and vorticity (color) at three phases of the acoustic cycle showing instantaneous (left) and phase-averaged (right) fields at 400 Hz out-of-phase forcing.

To help explain the prominence of the $m=-1$ and $m=1$ modes in the out-of-phase forcing cases, we perform the azimuthal mode decomposition on a model problem that is composed of two out-of-phase oscillating panels. This model problem represents a flapping motion similar to the transverse acoustic velocity field in the out-of-phase forcing case. This configuration captures $m=|1|$, non-axisymmetric motion while simplifying the geometry considerably. The difference between the oscillating planes and the out-of-phase acoustic forcing is the presence of swirl and helical fluid motion in the actual flow field. Figure 16 shows the scalar values of each half, where points on the left oscillate as a cosine of a set frequency, and points on the right oscillate with the same frequency but a phase difference of 180° .

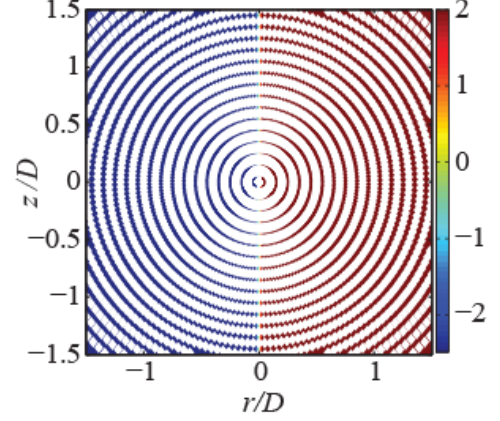


Figure 16: Oscillating planes of the model problem with white interpolation points.

The azimuthal mode decomposition of the model problem is plotted in Figure 17, which shows the mode strengths for modes $m=-10$ to $m=10$ at the frequency of oscillation. This configuration has strong peaks for modes $m=-1$ and $m=1$ while the other modes have lesser strength. In the oscillating panels case modes $m=1$ and $m=-1$ have the same magnitudes. Higher-order odd modes appear as well, but the mode strengths are much lower than the first helical modes. These higher order modes are most likely a manifestation of the step change between the two halves of the field, which leads to the Gibb's phenomena.

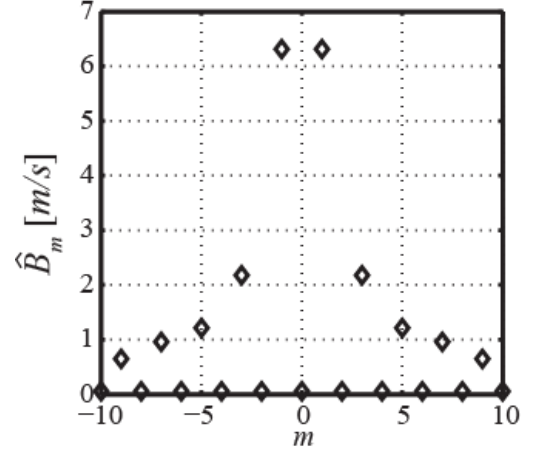


Figure 17: Mode strengths for model problem consisting of oscillating planes.

As shown in Figure 14 and Figure 17, modes $m=-1$ and $m=1$ are the strongest modes for the out-of-phase forcing and oscillating planes cases. This shows the similarity of the motion of the transverse acoustic velocity fluctuations in the out-of-phase forcing case to a bulk oscillatory motion in the field, described by the oscillating plates.

One difference between the oscillating planes and out-of-phase forcing cases is the phase difference between the $m=1$ and $m=-1$ modes. The phase difference between the $m=1$ and

$m=-1$ modes of the model problem is shown in Figure 18 in black squares, while the phase difference between these same modes of the 400 Hz and 800 Hz out-of-phase forcing data is shown in red circles and blue diamonds, respectively. The phase difference between modes $m=1$ and $m=-1$ in the oscillating planes case is zero. However, in the out-of-phase forcing data, the phase between modes $m=1$ and $m=-1$ is approximately 180° . The difference between the oscillating planes and the experimental results is most likely due to the swirling motion in the flow field. The swirl motion has a preferential direction, causing the helices in the flow field to not only wind but also rotate around the flow field, whereas in the oscillating planes there is no rotation.

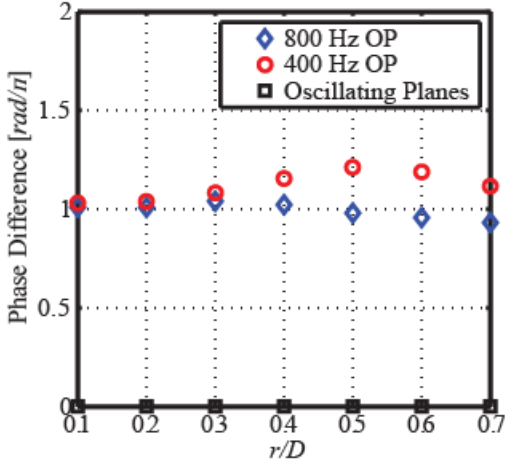


Figure 18: Phase difference (normalized by π) between modes $m=-1$ and $m=1$ for 800 Hz out-of-phase forcing (blue diamonds), 400 Hz out-of-phase forcing (red circles), and the oscillating plane model problem (black squares).

The response of the flow field to axisymmetric, or in-phase, forcing is quite different. Figure 19 shows the azimuthal mode decomposition of the fluctuating velocities at 400 Hz in-phase forcing. Inside the vortex breakdown bubble, at $r/D=0.2$, the response of the flow field is relatively small, and differences in the strength of the velocity fluctuations from the inherent instability are minimal; this was discussed in more detail in O'Connor and Lieuwen [29]. However, the response of the shear layers, at $r/D=0.4$ and $r/D=0.6$, is quite different in the in-phase forcing case than with out-of-phase forcing. In the presence of in-phase forcing, the response of the $m=0$ mode is quite strong at $x/D=0$ – several times stronger than the fluctuating energy in the other modes. This is a result of the axisymmetric forcing imposing an axisymmetric boundary condition at the vortex separation point, resulting in ring vortex shedding. This ring vortex can be seen in the velocity field visualization in Figure 20 for the axisymmetric forcing case.

However, the strength of the $m=0$ mode significantly decays downstream of the separation point and the strengths of the non-axisymmetric $m=1$ and $m=-1$ modes increase. This loss of axisymmetry is also evident in the flow visualization in

Figure 20, where the vortex “tilts” as it moves downstream in both the instantaneous and phase-averaged images. The fact that this tilting occurs in the phase-averaged images is indicative of the repeatability of this phenomenon. This non-axisymmetric behavior, even in the presence of axisymmetric acoustic forcing, is likely the result of the inherent non-axisymmetric instability characteristics of the flow field, as shown in Figure 11. The inherent instabilities have significant $m=-1$ and $m=-2$ content, and after the separation point where the axisymmetric boundary condition is imposed by the acoustic forcing, the inherent non-axisymmetric behavior is evident.

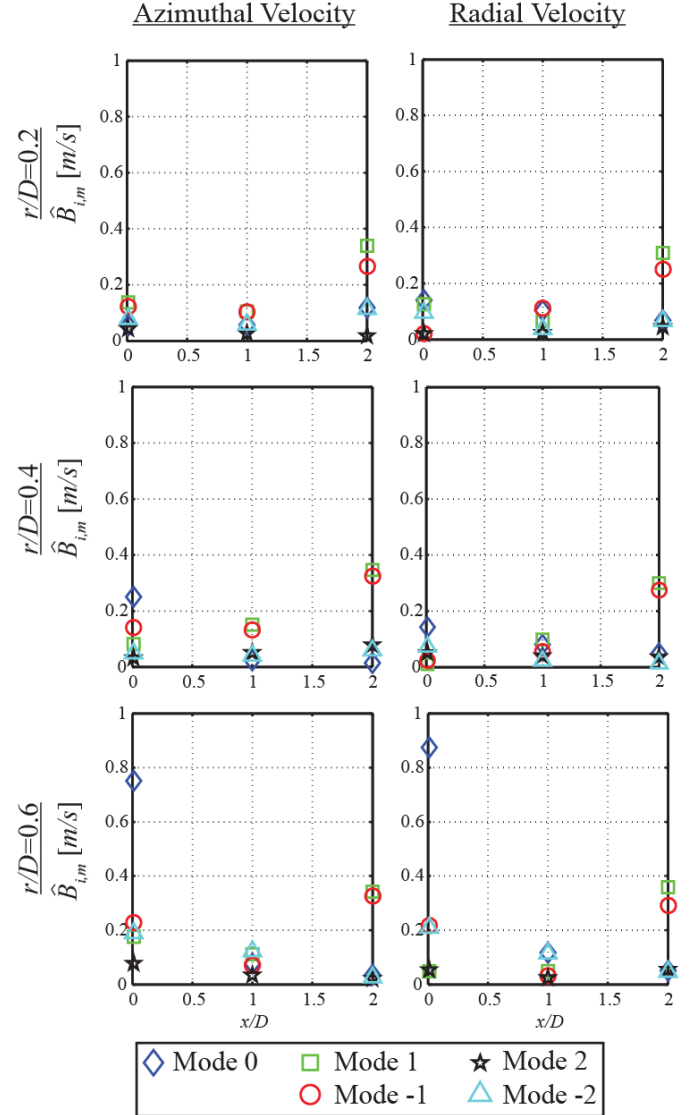


Figure 19: Azimuthal modes, $m=-2$ to $m=2$, at three radial locations for 400 Hz in-phase forcing.

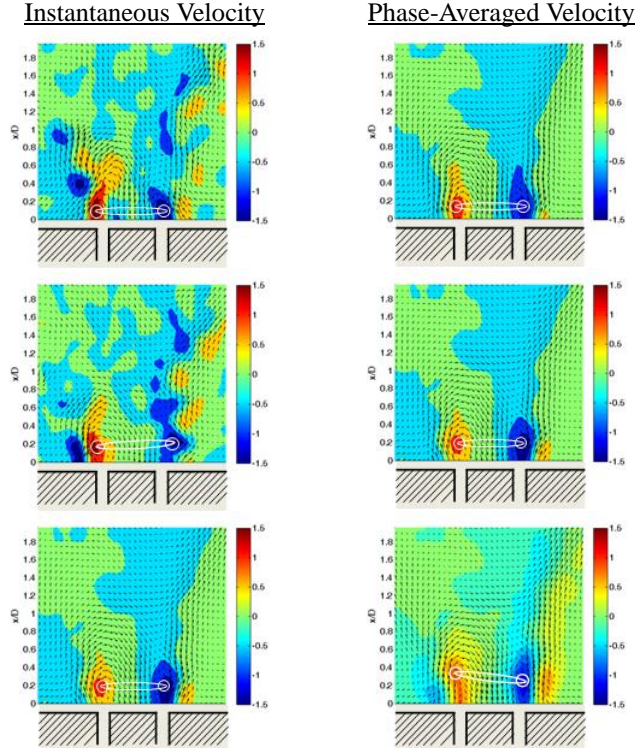


Figure 20. Normalized velocity (vectors) and vorticity (color) at three phases of the acoustic cycle showing instantaneous (left) and phase-averaged (right) fields at 400 Hz in-phase forcing.

Similar results were seen at 800 Hz at both in-phase and out-of-phase conditions. When comparing the same forcing conditions, there are not many differences between the 400 Hz and 800 Hz conditions. Forcing at 400 Hz generally leads to higher velocity fluctuation amplitudes but overall growth and decay of mode strength does not vary significantly.

CONCLUSIONS

This work has described both the time-averaged and fluctuating velocity fields of a transversely forced swirling annular jet. The results show that the jet is largely axisymmetric in the time-average. This was quantified using an azimuthal mode decomposition of the time-averaged velocity field. Axisymmetry is strongest at the jet exit and decreases as the flow progresses downstream as a result of the non-axisymmetric boundary conditions imposed by the combustor geometry. It was also shown that acoustic excitation does not significantly alter the time-averaged behavior of the strongly axisymmetric flow field.

The inherent instability modes of the jet are dominated by $m=-1$ and $m=-2$ in both the measurements and stability analysis. These results indicate that the vorticity fluctuations in the jet, driven by hydrodynamic instability, are non-axisymmetric.

Acoustic forcing is able to alter the dynamic behavior of the jet, and the response of the jet is largely dependent on the axisymmetry of the acoustic forcing condition. Non-

axisymmetric acoustic forcing leads to non-axisymmetric fluctuation in the $m=1$ and $m=-1$ modes throughout the flow field. Through the use of a model problem, it was shown that this $m=1$ and $m=-1$ modal content is due to both the non-axisymmetric acoustic velocity fluctuations and helical motion in the flow field. The axisymmetric forcing condition, however, results in strong axisymmetric motion at the dump plane, shown to be an $m=0$ mode resulting in a ring vortex roll-up. Further downstream, however, the $m=0$ mode decays and the $m=1$ and $m=-1$ modes increase in strength, resulting in a tilting of the vortex ring. This is likely a result of the natural non-axisymmetry of the flow field driving the dynamical behavior, even in the presence of acoustic forcing.

These results have important implications for flame response during transverse instabilities. Previous theoretical work has shown that the response of a time-averaged axisymmetric flame, as would be supported in this time-averaged axisymmetric flow field, does not respond to purely non-axisymmetric input disturbances, as would be driven by out-of-phase forcing, in the linear, compact flame regime [9, 47]. Despite the vortical velocity fluctuations in the flow field and resultant flame wrinkling, the net fluctuation in flame surface area over an acoustic cycle is zero. It has been shown that axisymmetric disturbances do result in net flame surface area fluctuations in these flames, although the non-axisymmetric behavior of the vortical velocity fluctuations further downstream of the dump plane may decrease the overall response of the flame. Future work will involve further investigation into the overall impact of this non-axisymmetric downstream development on flame response.

ACKNOWLEDGMENTS

This work has been partially supported by the US Department of Energy under contracts DEFG26-07NT43069 and DE-NT0005054, contract monitors Mark Freeman and Richard Wenglarz, respectively. Additional thanks to Tim Lieuwen and Vishal Acharya for their input to this work.

REFERENCES

1. Lieuwen T C and Yang V, *Combustion instabilities in gas turbine engines: Operational experience, fundamental mechanisms and modeling*, Progress in Astronautics and Aeronautics, American Institute of Aeronautics and Astronautics, Washington, DC (2005)
2. Rayleigh J W S B, *The Theory of Sound*, Macmillan, London, England (1896)
3. O'Connor J, Acharya V, Lieuwen T, "Transverse Combustion Instabilities: Acoustic, Fluid Mechanic, and Flame Processes" Progress in Energy and Combustion Science (**in press**) (2014)
4. O'Connor J and Lieuwen T, "Disturbance field characteristics of a transversely excited burner" Combustion Science and Technology **183**(5):427-443 (2011)

5. Hauser M, Lorenz M, Sattelmayer T, "Influence of transversal acoustic excitation of the burner approach flow on the flame structure" *Journal of Engineering for Gas Turbines and Power* **133**(4):041501 (2011)
6. Saurabh A, Steinert R, Moeck J P, Paschereit C O, "Swirl Flame Response to Traveling Acoustic Waves" ASME Turbo Expo Dusseldorf, Germany (2014)
7. Dawson J R and Worth N A, "Flame dynamics and unsteady heat release rate of self-excited azimuthal modes in an annular combustor" *Combustion and Flame* **161**(10):2565-2578 (2014)
8. Aguilar M, Malanoski M, Adhitya G, Emerson B, Acharya V, Noble D, Lieuwen T, "Helical Flow Disturbances in a Multi-Nozzle Combustor" ASME Turbo Expo Dusseldorf, Germany (2014)
9. Acharya V and Lieuwen T, "Response of Non-Axisymmetric Premixed, Swirl Flames to Helical Disturbances" ASME Turbo Expo, Dusseldorf, Germany (2014)
10. Staffelbach G, Gicquel L, Boudier G, Poinot T, "Large Eddy Simulation of self excited azimuthal modes in annular combustors" *Proceedings of the Combustion Institute* **32**(2):2909-2916 (2009)
11. Bauerheim M, Staffelbach G, Worth N, Dawson J, Gicquel L, Poinot T, "Sensitivity of LES-based harmonic flame response model for turbulent swirled flames and impact on the stability of azimuthal modes" *Proceedings of the Combustion Institute* (**in press**) (2014)
12. Kim K T, Lee J G, Quay B D, Santavicca D, "Experimental investigation of the nonlinear response of swirl-stabilized flames to equivalence ratio oscillations" *Journal of Engineering for Gas Turbines and Power* **133**(2):021502 (2011)
13. Bobusch B C, Ćosić B, Moeck J P, Paschereit C O, "Optical measurement of local and global transfer functions for equivalence ratio fluctuations in a turbulent swirl flame" *Journal of Engineering for Gas Turbines and Power* **136**(2):021506 (2014)
14. Ducruix S, Schuller T, Durox D, Candel S, "Combustion dynamics and instabilities: Elementary coupling and driving mechanisms" *Journal of Propulsion and Power* **19**(5):722-734 (2003)
15. Poinot T J, Trounev A C, Veynante D P, Candel S M, Esposito E J, "Vortex-driven acoustically coupled combustion instabilities" *Journal of Fluid Mechanics* **177**:265-292 (1987)
16. Altay H M, Speth R L, Hudgins D E, Ghoniem A F, "Flame-vortex interaction driven combustion dynamics in a backward-facing step combustor" *Combustion and Flame* **156**(5):1111-1125 (2009)
17. Hirsch C, Fanaca D, Reddy P, Polifke W, Sattelmayer T, "Influence of the swirler design on the flame transfer function of premixed flames" ASME Turbo Expo, Reno, NV (2005)
18. Palies P, Durox D, Schuller T, Candel S, "The combined dynamics of swirler and turbulent premixed swirling flames" *Combustion and Flame* **157**(9):1698-1717 (2010)
19. Paschereit C O, Gutmark E, Weisenstein W, "Coherent structures in swirling flows and their role in acoustic combustion control" *Physics of Fluids* (1994-present) **11**(9):2667-2678 (1999)
20. Thumuluru S K and Lieuwen T, "Characterization of acoustically forced swirl flame dynamics" *Proceedings of the Combustion Institute* **32**(2):2893-2900 (2009)
21. Blimbaum J, Zanchetta M, Akin T, Acharya V, O'Connor J, Noble D, Lieuwen T, "Transverse to longitudinal acoustic coupling processes in annular combustion chambers" *International Journal of Spray and Combustion Dynamics* **4**(4):275-298 (2012)
22. Yang V and Anderson W, *Liquid rocket engine combustion instability*, Progress in Astronautics and Aeronautics, American Institute of Aeronautics and Astronautics, (1995)
23. Hall M, "Vortex breakdown" *Annual Review of Fluid Mechanics* **4**(1):195-218 (1972)
24. Leibovich S, "Vortex stability and breakdown-Survey and extension" *AIAA Journal* **22**(9):1192-1206 (1984)
25. Brown G and Lopez J, "Axisymmetric vortex breakdown Part 2. Physical mechanisms" *Journal of Fluid Mechanics* **221**:553-576 (1990)
26. Lucca-Negro O and O'Doherty T, "Vortex breakdown: A review" *Progress in Energy and Combustion Science* **27**(4):431-481 (2001)
27. Candel S, Durox D, Schuller T, Bourgouin J, Moeck J, "Dynamics of Swirling Flames" *Annual Review of Fluid Mechanics* **46**:147-173 (2014)
28. Gursul I, "Effect of nonaxisymmetric forcing on a swirling jet with vortex breakdown" *Journal of Fluids Engineering* **118**(2):316-321 (1996)
29. O'Connor J and Lieuwen T, "Recirculation zone dynamics of a transversely excited swirl flow and flame" *Physics of Fluids* (1994-present) **24**(7):075107 (2012)
30. Bellows B D, Neumeier Y, Lieuwen T, "Forced response of a swirling, premixed flame to flow disturbances" *Journal of Propulsion and Power* **22**(5):1075-1084 (2006)
31. Steinberg A, Boxx I, Stöhr M, Carter C, Meier W, "Flow-flame interactions causing acoustically coupled heat release fluctuations in a thermo-acoustically unstable gas turbine model combustor" *Combustion and Flame* **157**(12):2250-2266 (2010)
32. O'Connor J and Lieuwen T, "Further characterization of the disturbance field in a transversely excited swirl-stabilized flame" *Journal of Engineering for Gas Turbines and Power* **134**(1):011501 (2012)

33. Kusek S, Corke T, Reisenthel P, "Seeding of helical modes in the initial region of an axisymmetric jet" *Experiments in Fluids* **10**(2-3):116-124 (1990)
34. Reynolds W, Parekh D, Juvet P, Lee M, "Bifurcating and blooming jets" *Annual Review of Fluid Mechanics* **35**(1):295-315 (2003)
35. Liang H and Maxworthy T, "An experimental investigation of swirling jets" *Journal of Fluid Mechanics* **525**:115-159 (2005)
36. Loiseleux T, Chomaz J, Huerre P, "The effect of swirl on jets and wakes: Linear instability of the Rankine vortex with axial flow" *Physics of Fluids* (1994-present) **10**(5):1120-1134 (1998)
37. Gallaire F and Chomaz J-M, "Mode selection in swirling jet experiments: a linear stability analysis" *Journal of Fluid Mechanics* **494**:223-253 (2003)
38. Gallaire F and Chomaz J-M, "Instability mechanisms in swirling flows" *Physics of Fluids* (1994-present) **15**(9):2622-2639 (2003)
39. Manoharan K, Hansford S, O'Connor J, Hemchandra S, "Instability Mechanism in a Swirl Flow Combustor: Precession of Vortex Core and Influence of Density Gradient" *ASME Turbo Expo*, Montreal, Canada (2014)
40. Huerre P and Monkewitz P, "Absolute and convective instabilities in free shear layers" *Journal of Fluid Mechanics* **159**:151-168 (1985)
41. Olendraru C and Sellier A, "Viscous effects in the absolute-convective instability of the Batchelor vortex" *Journal of Fluid Mechanics* **459**:371-396 (2002)
42. Olendraru C, Sellier A, Rossi M, Huerre P, "Inviscid instability of the Batchelor vortex: Absolute-convective transition and spatial branches" *Physics of Fluids* (1994-present) **11**(7):1805-1820 (1999)
43. Oberleithner K, Sieber M, Nayeri C, Paschereit C, Petz C, Hege H-C, Noack B, Wygnanski I, "Three-dimensional coherent structures in a swirling jet undergoing vortex breakdown: stability analysis and empirical mode construction" *Journal of Fluid Mechanics* **679**:383-414 (2011)
44. Lefebvre A H, *Gas turbine combustion*, CRC Press, Hoboken, NJ (2010)
45. O'Connor J, Worth N A, Dawson J R, "Flame and Flow Dynamics of a Self-Excited, Standing Wave Circumferential Instability in a Model Annular Gas Turbine Combustor" *ASME Turbo Expo*, (2013)
46. Blackstock D T, *Fundamentals of physical acoustics*, John Wiley & Sons, New York, NY (2000)
47. Acharya V, Shin D-H, Lieuwen T, "Swirl effects on harmonically excited, premixed flame kinematics" *Combustion and Flame* **159**(3):1139-1150 (2012)
48. Batchelor G and Gill A, "Analysis of the stability of axisymmetric jets" *Journal of Fluid Mechanics* **14**(04):529-551 (1962)
49. Deissler R J, "The convective nature of instability in plane Poiseuille flow" *Physics of Fluids* (1958-1988) **30**(8):2303-2305 (1987)
50. Cala C, Fernandes E, Heitor M, Shtork S, "Coherent structures in unsteady swirling jet flow" *Experiments in Fluids* **40**(2):267-276 (2006)
51. Malik, Mujeeb R., Thomas A. Zang, and M. Yousuff Hussaini. "A spectral collocation method for the Navier-Stokes equations." *Journal of Computational Physics* 61.1 (1985): 64-88
52. Boyd, John P. *Chebyshev and Fourier spectral methods*. Courier Dover Publications, 2001.